A Monte Carlo collision model for the particle-in-cell method: applications to argon and oxygen discharges

V. Vahedi [a,b], M. Surendra [c]

[a] *Department of Electrical Engineering and Computer Science, University of California, Berkeley, CA 94720, USA*
[b] *Lawrence Livermore National Laboratory, Livermore, CA 94550, USA*
[c] *IBM T.J. Watson Research Center, Yorktown Heights, NY 10598, USA*

Abstract

In order to use particle-in-cell (PIC) simulation codes for modeling collisional plasmas and self-sustained discharges, it is necessary to add interactions between charged and neutral particles. In conventional Monte Carlo schemes the time or distance between collisions for each particle is calculated using random numbers. This procedure allows for efficient algorithms but is not compatible with PIC simulations where the charged particle trajectories are all integrated simultaneously in time. A Monte Carlo collision (MCC) package including the null collision method has been developed, as an addition to the usual PIC charged particle scheme which will be discussed here. We will also present results from simulations of argon and oxygen discharges, and compare our argon simulation results with experimental measurements.

1. Introduction

RF and DC glow discharges are used widely in the microelectronics industry. Self-consistent fluid equations have been used by Graves and Jensen [1], Boeuf [2] and Gogolides et al. [3] to study the structural features of RF and DC glows. However, since these discharges are inherently complex, and the particle velocity distributions can be non-Maxwellian, there has been a considerable effort to develop self-consistent kinetic models with no assumptions about the distribution functions. Monte Carlo methods have been used extensively in swarm simulations [4–9]. The conventional method of calculating the time between collisions for each particle using a random number can be generalized into efficient algorithms, especially when the null collision method is also used [6,10]. However, this conventional method is not compatible with PIC simulations where all the charged particle trajectories are integrated simultaneously in time.

Hence, we have developed a Monte Carlo collision (MCC) package, including the null collision method [11,14,15] as an addition to the usual PIC charged particle scheme as shown in Fig. 1. A thorough description of the PIC technique can be found in Birdsall and Langdon (1985, 1991) [16]. Vahedi et al. [15] also analyzed the PIC techniques and discussed some of the main issues in PIC simulations of weakly ionized collisional discharges. Here we will discuss only the MCC package. The full three-dimensional character of a collision is modeled with three velocity components. The neutral particles can be assumed, for simplicity, to have a uniform density between the boundaries with a Maxwellian velocity distribution. The model is still valid if the
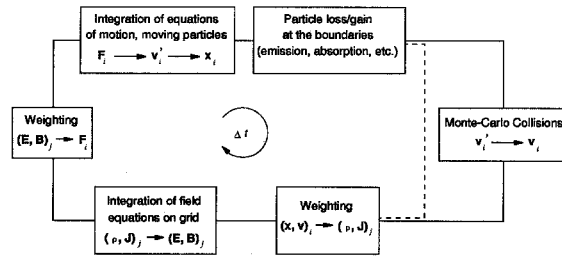
Fig. 1. The flow chart for an explicit PIC scheme with the addition of the collision handler, called PIC-MCC.

neutral density is a function of position and time, as will be discussed. In principle, this scheme can also be extended to model Coulomb collisions between charged particles.

One of the main reasons for simulating weakly ionized collisional plasmas using the PIC-MCC scheme is to obtain the self-consistent electron energy distribution functions (EEDFs) in these discharges. Bi-Maxwellian EEDFs were measured experimentally in argon RF discharges at 13.56 MHz by Godyak et al. [17]. The observed EEDFs at low pressures had very-low energy and high energy components. We show particle-in-cell Monte Carlo (PIC-MCC) simulations which produce the same EEDFs. Excellent agreement is obtained between the effective low and high electron temperatures in simulations and those measured in the laboratory. We will also present results from simulations of oxygen discharges and show EEDFs and density profiles for various species.

2. General description of the mcc model

We first describe the Monte Carlo Collision model and then the addition of a null collision process as a way to optimize the general MCC scheme. The null collision process can be especially important in modeling Coulomb collisions. We define a background species as a species whose density can be described as a function of time and space. Particle species, on the other hand, are characterized by super-particles whose distribution functions evolve temporally and spatially as the super-particles move in the system in response to the local electric field when they are charged.

Assume the particle species s has N types of collisions with a target species. The target species could be a background species or another particle species. The kinetic energy of the ith particle of the incident s species is given by

$$\mathcal{E}_i = \tfrac{1}{2}m_s v_i^2 = \tfrac{1}{2}m_s(v_{ix}^2 + v_{iy}^2 + v_{iz}^2)$$ (1)

This energy is needed in calculating the collision cross sections. The total collision cross section $\sigma_T(\mathcal{E}_i)$ is the sum

$$\sigma_T(\mathcal{E}_i) = \sigma_1(\mathcal{E}_i) + \cdots + \sigma_N(\mathcal{E}_i)$$ (2)

where $\sigma_j(\mathcal{E}_i)$, for $1 \leq j \leq N$, is the cross section of the jth type of collision between the s species and the target species. The collision probability for the ith particle is calculated, based on the distance $\Delta s_i = v_i \Delta t$ traveled in each time step Δt, to be

$$P_i = 1 - \exp(-\Delta s_i \sigma_T(\mathcal{E}_i) n_t(\mathbf{x}_i)) = 1 - \exp(-\Delta t v_i \sigma_T(\mathcal{E}_i) n_t(\mathbf{x}_i))$$ (3)

where $n_t(\mathbf{x}_i)$ is the local density of the target species at the position of the ith particle.

A collision takes place if a uniformly distributed random number on the interval [0, 1] is less than P_i. If a collision occurs, then another random number is chosen to determine the type of collision. The energy and
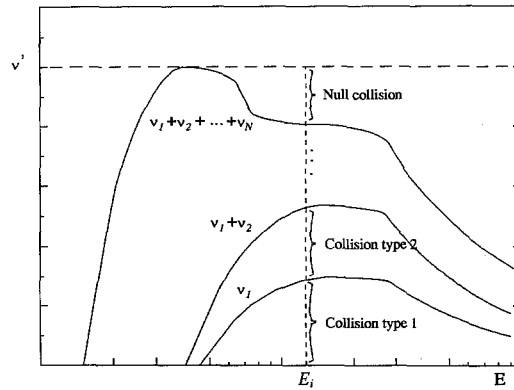
Fig. 2. The addition of the null collision process results in a constant collision frequency over all energies.

scattering angle of the particle and other fragments involved in the collision are then determined, as we will see later, based on the model assumed for that type of collision.

A collision is assumed to take place in the time interval $[t, t + \Delta t]$ at the current position of the ith particle, $\mathbf{x}_i(t)$. In a time-centered PIC scheme, the velocities, $\mathbf{v}_i(t + \Delta t)$, are generated by interpolating the local electric field, $\mathbf{E}_i(t)$, hence P_i has numerical noise comparable to the local truncation error of the PIC scheme. If Δx is chosen for the desired PIC accuracy, no further constraint is present with MCC.

The time step, Δt, determines how often to check for a collision and can affect the accuracy of the collision model. For any finite Δt, $P_i < 1$. In an electron scattering collision, for example, the energy of the scattered electron remains roughly constant. Then the probability for n collisions in the same Δt is roughly P_i^n. Since MCC allows only one collision per particle per Δt, the generated error, which we define as the number of missed collisions in Δt for a given particle, is

$$r \sim \sum_{k=2}^{\infty} P_i^k = \frac{P_i^2}{1 - P_i} \tag{4}$$

An error of $r < 0.01$ requires $P_i < 0.095$, i.e. the time step Δt should be set so that $\Delta s_i \sigma_T(\mathcal{E}_i) n_t(\mathbf{x}_i)$ would be less than or equal to 0.1.

This scheme is compatible with PIC since the position and velocity of particles are advanced each time step. However, it is obvious that calculating P_i for all the particles each time step can be computationally very expensive, requiring looking up every particle's kinetic energy. This look-up can be avoided by choosing a constant collision frequency ν' such that

$$\nu' = \max_{\mathbf{x}, \mathcal{E}}(n_t \sigma_T v) = \max_{\mathbf{x}}(n_t) \max_{\mathcal{E}}(\sigma_T v) \tag{5}$$

In a sense all we have done is to introduce another collisional process with a collision frequency which, when it is added to the total collision frequency $n_t(\mathbf{x})\sigma_T(\mathcal{E})v$, gives a constant value over all $\mathbf{x}$ and $\mathcal{E}$. This collisional process is called the *null collision* since no real interaction occurs. Note that typically the target particles are assumed to be uniformly distributed in the system as a background species with a constant n_t, in which case it is only necessary to obtain the maximum over $\mathcal{E}$ as graphically shown in Fig. 2. However, in the case of, for example, electron–ion recombination, the density of the target particles (namely ions) is typically a function of position and time, which would make it necessary to obtain the maximum over $\mathbf{x}$ at each time step as well.

The maximum fraction of the total number of particles in the simulation which experience collisions is then given by

$$P_{null} = 1 - \exp(-\nu'\Delta t) \tag{6}$$

The colliding particles are chosen randomly (eliminating duplicates), and each particle is checked for type of collision, see Fig. 2, using

$$
\begin{aligned}
R &\le \nu_1(\mathcal{E}_i)/\nu' && \text{(Collision type 1)} \\
\nu_1(\mathcal{E}_i)/\nu' < R &\le (\nu_1(\mathcal{E}_i) + \nu_2(\mathcal{E}_i))/\nu' && \text{(Collision type 2)} \\
&\vdots \\
\Sigma_{j=1}^{N}\nu_j(\mathcal{E}_i)/\nu' &< R && \text{(Null collision)}
\end{aligned}
$$

where R is a random number ($R \in [0,1]$).

The computational efficiency of this method over the standard method depends on P_{null}. For a simulation with N_s particles, the standard method requires N_s evaluations of P_i whereas the null method requires only $N_s P_{null}$ evaluations of P_i. Note that each evaluation of P_i includes calculation of particle energy, $\mathcal{E}_i$, collision frequencies, $\nu_j(\mathcal{E}_i)$ for $1 \le j \le N$, and several other floating point operations. Typically P_{null} is on the order of 10^{-2}, so the computational saving can be quite significant.

3. Collision types

Typical laboratory gas discharges contain many species, and there are various reactions among these species. Bell [18] lists over thirty reactions in an oxygen discharge, and the list is by no means exhaustive. In studying and modeling these discharges we have taken a subset of these reactions for a few species to study each gas and make some comparisons. In each case, the chosen reactions were selected so that the system would model a self-sustained and self-consistent discharge. In most cases the selected reactions have the largest reaction rates which make them the best candidates. The two gases discussed here are argon, an electropositive atomic gas, and oxygen, an electronegative molecular gas.

3.1. Argon

The collision model for argon described below has been successfully used to RF capacitively coupled discharges [15]. Reactions in the simple argon model are

$$
\begin{aligned}
&(1)\ e + Ar \longrightarrow e + Ar && \text{(Elastic Scattering)} \\
&(2)\ e + Ar \longrightarrow e + Ar^* && \text{(Excitation)} \\
&(3)\ e + Ar \longrightarrow e + Ar^+ + e && \text{(Ionization)} \\
\\
&(4)\ Ar^+ + Ar \longrightarrow Ar + Ar^+ && \text{(Charge Exchange)} \\
&(5)\ Ar^+ + Ar \longrightarrow Ar^+ + Ar && \text{(Elastic Scattering)}
\end{aligned}
$$

Here we assume that the argon gas (the neutral species) is maintained uniformly in space, i.e., the neutral particles are not followed as particles, and we assume two types of collisions for the ions. (The separation between charge exchange and elastic collisions for ions will be discussed in Section 3.1.2.) Note that in some electron–neutral collisions, the target neutral particles gain some energy or leave the collision in an excited state. However, the dominant electron–neutral collisions will be between the electrons and the background low temperature gas particles if the population of the excited and/or energetic neutrals is low enough, which is assumed to be the case. The neutral species is also assumed to have a Maxwellian velocity distribution at the gas temperature (e.g., $T_N = 0.026$ eV). Hence, the neutrals are much less energetic than an average electron in a system, but because of the large neutral-to-electron mass ratio, the momentum of the neutral remains roughly unchanged in most electron–neutral collisions.
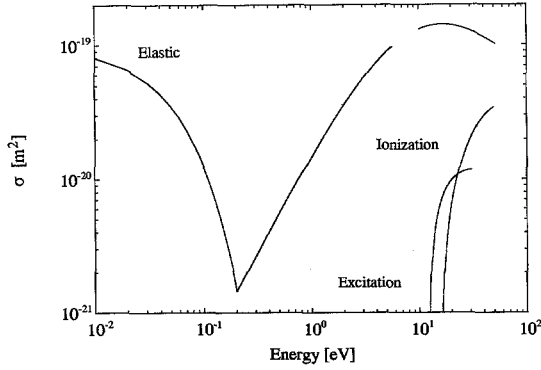
Fig. 3.

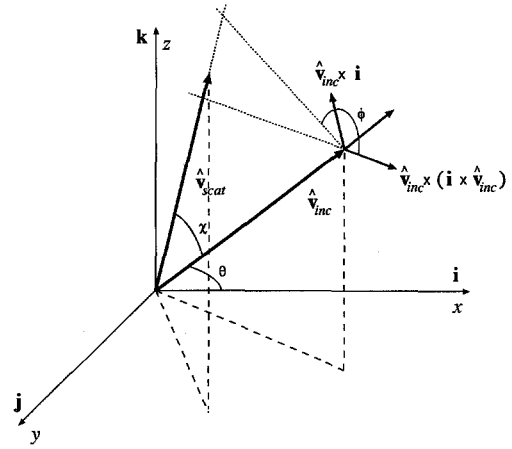Fig. 4.

Fig. 3. The electron–neutral cross sections in argon.

Fig. 4. Vector diagram for scattering collisions.

3.1.1. Electron–neutral collisions

The electron–neutral cross sections in the model are the same as the ones used by Surendra, Graves and Jellum (1990) [12] as shown in Fig. 3. In an electron–neutral elastic collision, the incident electron scatters through an angle χ which we determine with an approximate differential cross section of the form [11]

$$\frac{\sigma(\mathcal{E},\chi)}{\sigma(\mathcal{E})} = \frac{\mathcal{E}}{4\pi[1 + \mathcal{E}\sin^2(\chi/2)]\ln(1+\mathcal{E})}$$ (7)

where $\mathcal{E}$ is the energy of the incident electron in electronvolts. This can be solved for $\cos\chi$ from

$$R = \frac{\int_0^\chi \sigma(\mathcal{E},\chi)\sin\chi d\chi}{\int_0^\pi \sigma(\mathcal{E},\chi)\sin\chi d\chi}$$ (8)

where R is a random number ($R \in [0,1]$) to produce

$$\cos\chi = \frac{2 + \mathcal{E} - 2(1+\mathcal{E})^R}{\mathcal{E}}$$ (9)

We use Eq. (9) to determine the electron scattering angle for all types of electron–neutral collisions. For energetic incident electrons, Eq. (9) gives mostly small scattering angles (forward scattering) whereas, for low energy electrons, the scattering is more isotropic. The azimuthal scattering angle ϕ, is uniformly distributed on the interval $[0,2\pi]$, and is determined by

$$\phi = 2\pi R$$ (10)

where R is another random number ($R \in [0,1]$). Once χ and ϕ are known, the direction of the scattered velocity is obtained by geometric considerations. In Fig. 4 $\hat{v}_{inc}$ and $\hat{v}_{scat}$ are unit vectors parallel to the incident and scattered velocities, respectively. $\hat{v}_{scat}$ is related to $\hat{v}_{inc}$ by

$$\hat{v}_{scat} = \hat{v}_{inc}\cos\chi + \hat{v}_{inc} \times i\frac{\sin\chi\sin\phi}{\sin\theta} + \hat{v}_{inc} \times (i \times \hat{v}_{inc})\frac{\sin\chi\cos\phi}{\sin\theta}$$ (11)

where θ is given by $\cos\theta = \mathbf{v}_{inc} \cdot \hat{\mathbf{i}}$. Scattered velocity components can then be determined by taking the projection of $\hat{\mathbf{v}}_{scat}$ on the coordinate axes [13].

Once the scattering angle χ is determined, we can calculate the energy loss of the electron in a scattering event from [22]

$$\Delta\mathcal{E} = \frac{2m}{M}(1 - \cos\chi) \tag{12}$$

where m is the electron mass and M is the mass of the neutral. Although this energy loss is small because of the mass ratio, it is the only energy loss mechanism for the low energy electrons with energies less than the typical excitation and ionization threshold energies. In an argon discharge, however, this energy loss is not very significant because of the Ramsauer minimum in the scattering cross section; see Fig. 3.

In an excitation collision, the incident electron loses the excitation threshold energy of 11.55 eV and is scattered through an angle χ determined by Eq. (9). In this simple model, the excited atoms are not followed and a very short decay time is assumed for the excited states. This assumption is not accurate for all the excited states. In the future, as the model becomes more sophisticated, we intend to follow meta-stables as another particle species and allow them to be ionized. For now, the excitation reaction serves only as an energy-sink for the electrons.

In an ionizing event, an electron–ion pair is created, and the energy balance equation becomes

$$\mathcal{E}_{scat} + \mathcal{E}_{ej} + \mathcal{E}_i = \mathcal{E}_{inc} + \mathcal{E}_N - \mathcal{E}_{ion} \tag{13}$$

where $\mathcal{E}_{scat}$, $\mathcal{E}_{ej}$, and $\mathcal{E}_{inc}$ are energies of the scattered, ejected and incident electrons, respectively. $\mathcal{E}_i$ and $\mathcal{E}_N$ are the energies of the created ion and the target neutral atom, and $\mathcal{E}_{ion}$ is the ionization threshold energy.

Because of the large ion-to-electron mass ratio, we can assume that the momentum of the incident electron is much less than the momentum of the neutral atom. In other words, the incident electron strips an electron off the neutral, and the neutral becomes an ion, continuing on its trajectory virtually undisturbed. This assumption allows us to rewrite Eq. (13) as

$$\mathcal{E}_{scat} + \mathcal{E}_{ej} = \mathcal{E}_{inc} - \mathcal{E}_{ion} \tag{14}$$

$$\mathcal{E}_i = \mathcal{E}_N \tag{15}$$

We now need to find an algorithm to partition the remaining energy of the incident electron between the scattered and ejected electrons, Eq. (14). The simplest way would be to divide the remaining energy equally between the two electrons. A more detailed treatment can be found in Opal et al. (1971) [23] as described by Surendra et al. (1990) [11]. A simplified form of the differential ionization cross section is taken to be of the form [23]

$$S(\mathcal{E}_{inc}, \mathcal{E}_{ej}) = \frac{A(\mathcal{E}_{inc})}{\mathcal{E}_{ej}^2 + B^2(\mathcal{E}_{inc})} \tag{16}$$

The function $A(\mathcal{E}_{inc})$ is determined from

$$\sigma_{ion}(\mathcal{E}_{inc}) = \int_0^{(\mathcal{E}_{inc} - \mathcal{E}_{ion})/2} S(\mathcal{E}_{inc}, \mathcal{E}_{ej}) \, d\mathcal{E}_{ej} \tag{17}$$

to be

$$A(\mathcal{E}_{inc}) = \frac{\sigma_{ion} B(\mathcal{E}_{inc})}{\arctan\{[\mathcal{E}_{inc} - \mathcal{E}_{ion}]/[2B(\mathcal{E}_{inc})]\}} \tag{18}$$
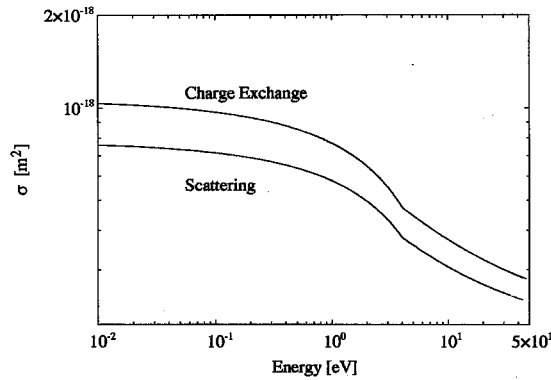
Fig. 5. The ion–neutral cross sections in argon.

This equation can be solved for $\mathcal{E}_{ej}$, by inverting the distribution,

$$R = \frac{\int_0^{\mathcal{E}_{ej}} S(\mathcal{E}_{inc}, \mathcal{E}'_{ej}) \, d\mathcal{E}'_{ej}}{\int_0^{\mathcal{E}_{ej}^{max}} S(\mathcal{E}_{inc}, \mathcal{E}'_{ej}) \, d\mathcal{E}'_{ej}} \tag{19}$$

where $\mathcal{E}_{ej}^{max} = (\mathcal{E}_{inc} - \mathcal{E}_{ion})/2$, and R is a random number, $(R \in [0, 1])$. Hence

$$\mathcal{E}_{ej} = B(\mathcal{E}_{inc}) \tan \left[R \arctan \left(\frac{\mathcal{E}_{inc} - \mathcal{E}_{ion}}{2B(\mathcal{E}_{inc})} \right) \right] \tag{20}$$

where $B(\mathcal{E}_{inc})$ is a known function [23] (e.g., for argon, $B(\mathcal{E}_{inc}) \simeq 10$ eV over a range of 1–70 eV). Eq. (20) is the energy partition function which allows us to divide the remaining energy of the incident electron between the scattered and ejected electrons.

Note that when the energy of the incident electron is just above the threshold, (i.e., $(\mathcal{E}_{inc} - \mathcal{E}_{ion})/(2B(\mathcal{E}_{inc}) \ll 1$), Eq. (20) reduces to

$$\mathcal{E}_{ej} \simeq R(\frac{\mathcal{E}_{inc} - \mathcal{E}_{ion}}{2}) \tag{21}$$

which means that on average the remaining energy is divided equally between the two electrons. Eq. (20) can also be used, with appropriate modifications, for other collision mechanisms such as electron impact detachment for negative ions.

After the energy assignment, each of the scattered and ejected electrons scatters through angles χ and ϕ determined by Eqs. (9) and (10). Now that the electrons are taken care of, we must bring our attention to the created ion. As we saw in Eq. (15), the created ion takes the energy and direction of the neutral atom before the collision. Therefore we can pick a neutral atom from a 3V Maxwellian distribution at the temperature T_N, and call it an ion. This gives a very low-temperature Maxwellian source for the ions in the system. This is important in analyzing ion dynamics and ion–neutral collisions.

3.1.2. Ion–neutral collisions

Fig. 5 shows the ion–neutral cross sections used in the model [24]. In electron–neutral collisions, the assumption that the neutrals were stationary as compared with the incident electrons made the collision models very simple. In ion–neutral collisions, we cannot make the same assumption; in the bulk plasma the ions and neutral atoms typically have similar velocities. However, in a reference frame in which the neutral atom is at rest, for each ion collision, we can choose a neutral at random from a 3V Maxwellian distribution at T_N, and

subtract its velocity from the velocity of the incident ion. Note that the incident ions in this frame can have higher speeds which affect the type of collision they suffer. Hence, each ion selected to undergo a collision, in the null collision scheme, must be transferred into this frame, go through a collision, and be transferred back into the laboratory frame by adding the chosen neutral velocity to its velocity.

In a charge exchange collision, an electron is assumed to hop from the neutral onto the ion, causing the neutral to become an ion with zero velocity in the neutral frame. After transferring back to the laboratory frame, the new ion leaves the collision with the velocity of the incident neutral, and the new neutral takes the velocity of the incident ion.

The ion–neutral elastic scattering events are assumed to be hard sphere collisions in which the energy of the scattered ions are determined by [22]

$$\mathcal{E}_{scat} = (1 - \alpha_L)\mathcal{E}_{inc} \tag{22}$$

where $\mathcal{E}_{inc}$ and $\mathcal{E}_{scat}$ are the energies of incident and scattered ions, respectively. The energy loss factor, α_L, is given by [22]

$$\alpha_L = \frac{2m_1 m_2}{(m_1 + m_2)^2}(1 - \cos\Theta) \tag{23}$$

where m_1 and m_2 are the ion and neutral masses and Θ is the scattering angle in the center-of-mass frame. For $m_1 = m_2$,

$$\Theta = 2\chi \tag{24}$$

where χ is the scattering angle in the laboratory frame; hence $\alpha_L = \sin^2\chi$ and

$$\mathcal{E}_{scat} = \mathcal{E}_{inc}\cos^2\chi \tag{25}$$

The angle χ can be determined by assuming scattering to be uniform and isotropic in the center-of-mass frame which gives

$$\cos\Theta = 1 - 2R \tag{26}$$

where R is a random number ($R \in [0, 1]$). For $\Theta = 2\chi$, we have

$$\cos\chi = \sqrt{1 - R} \tag{27}$$

The azimuthal scattering angle ϕ is determined with Eq. (10). As in charge exchange, the ion must be transferred into a frame in which the neutral particle is stationary, scattered, and transferred back to the laboratory frame.

The separation between charge exchange and elastic scattering for identical collision partners is an artificial construct which is useful since it parallels collisions between nonidentical particles. Nonetheless, care must be taken to ensure that the prescribed cross sections for each process are consistent with the momentum transfer cross section for the ions. The more proper approach would be to use the differential cross section for ion–neutral collisions in order to determine the scattering angle which would then be used to determine the ion-energy loss from Eq. (25). Vestal et al. [25] used crossed-beam measurements to determine the differential cross sections for low-energy $Ar^+ - Ar$ collisions. Their measurements show that most of the scattering angles are either close to 180 degrees in the center-of-mass (which is what we call charge exchange), or close to zero degrees (small angle scattering). This suggests that the average ion angle calculated with the differential cross section of Vestal et al. [25] may be smaller than the average angle obtained using isotropic hard sphere collisions.

Unfortunately, measurements of differential cross sections for most ion–neutral collisions are not available, and the measurements of Vestal et al. [25] were made in argon for relative ion energies of 2–20 eV. However, one can attempt to fit the measured differential cross section with a function of the form

$$\frac{\sigma(\mathcal{E},\Theta)}{A\sigma(\mathcal{E})} = \frac{a(\mathcal{E})}{[1 + \cos\Theta + a(\mathcal{E})][1 - \cos\Theta + a(\mathcal{E})]} \tag{28}$$

where $\mathcal{E}$ is the relative energy of the incident ion, Θ is the scattering angle in the center-of-mass, $\sigma(\mathcal{E})$ is the total ion–neutral cross section, and $a(\mathcal{E})$ is a dimensionless fitting parameter. The parameter A is a normalizing factor and is obtained from

$$\sigma(\mathcal{E}) = 2\pi \int\limits_0^\pi \sigma(\mathcal{E},\Theta)\sin\Theta d\Theta.$$

Eq. (28) is plotted in Fig. 6 for several values of a. According to the measurements of Vestal et al. [25], a is on the order of 10^{-3} in argon over relative energies of 2–20 eV.

The differential cross section in Eq. (28) can be used to determine the scattering angle using

$$R = \frac{\int_0^\Theta \sigma(\mathcal{E},\Theta)\sin\Theta d\Theta}{\int_0^\pi \sigma(\mathcal{E},\Theta)\sin\Theta d\Theta} \tag{29}$$

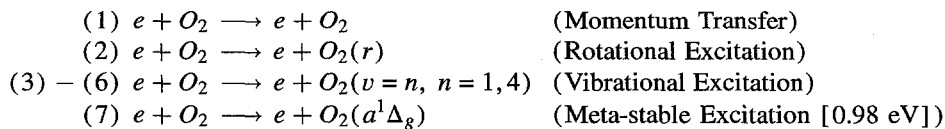where R is a random number ($R \in [0,1]$). Solving this for the scattering angle Θ in the center-of-mass gives

$$\cos\Theta = (1 + a)\frac{1 - (a/(a+2))^{1-2R}}{1 + (a/(a+2))^{1-2R}} \tag{30}$$

Eq. (30) is plotted in Fig. 7 for various values of a and compared with the hard sphere isotropic limit in Eq. (26). As expected, for small values of a most of the ion–neutral collisions are either forward or backward scatterings in the center-of-mass, whereas for larger values of a the distribution approach the isotropic limit where all angles are equally likely.

The fit to the differential cross section given in Eq. (28) has not been verified for higher relative ion energies, however, it is clear that the same analysis can be done with other more exact fits to obtain the scattering angle. Presently, we have the two separate reactions for argon, and are in the process of incorporating the differential scattering cross sections in our model.

3.2. Oxygen

Reactions in our oxygen model are:

$$
\begin{array}{lll}
(1) & e + O_2 \longrightarrow e + O_2 & \text{(Momentum Transfer)} \\
(2) & e + O_2 \longrightarrow e + O_2(r) & \text{(Rotational Excitation)} \\
(3) - (6) & e + O_2 \longrightarrow e + O_2(v = n, \ n = 1, 4) & \text{(Vibrational Excitation)} \\
(7) & e + O_2 \longrightarrow e + O_2(a^1\Delta_g) & \text{(Meta-stable Excitation [0.98 eV])}
\end{array}
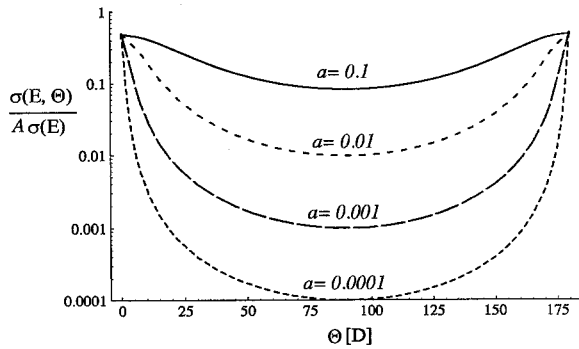$$

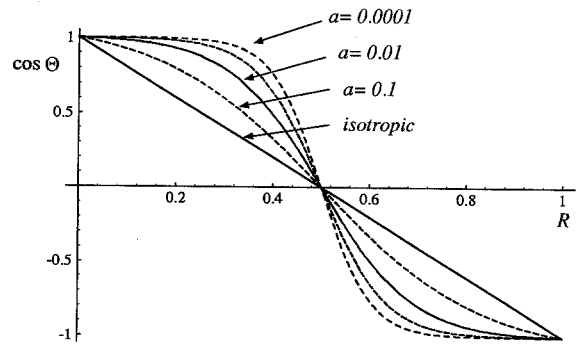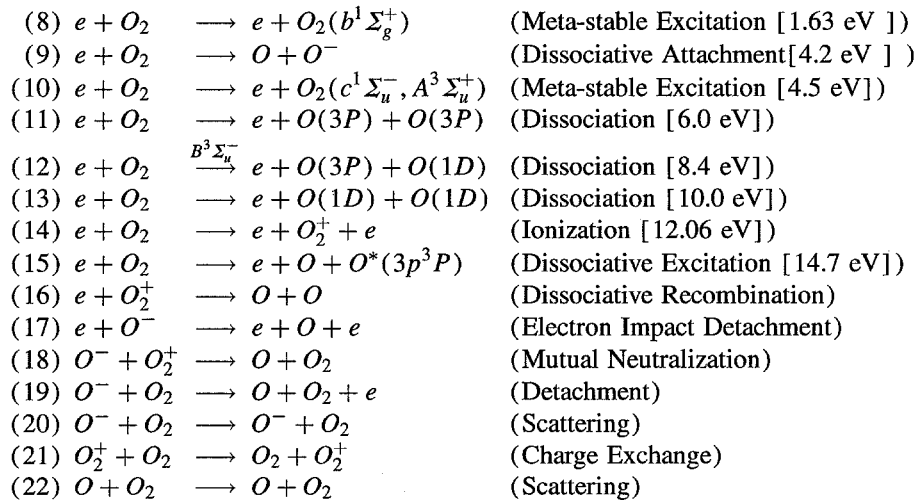Fig. 6.   Fig. 7.

Fig. 6. Analytic fit to the measured differential cross section for ion–neutral collisions. The analytic fit is plotted for several values of the dimensionless fitting parameter a.

Fig. 7. Distribution of scattering angles in the center-of-mass obtained with our fit to the differential scattering cross section for various values of the dimensionless fitting parameter a, where R is a random number. For small values of a most of the collisions are either forward or backward scatterings in the center-of-mass, whereas at larger values of a the distribution approaches the isotropic limit.

$$(8) \quad e + O_2 \longrightarrow e + O_2(b^1\Sigma_g^+) \qquad \text{(Meta-stable Excitation [1.63 eV])}$$
$$(9) \quad e + O_2 \longrightarrow O + O^- \qquad \text{(Dissociative Attachment[4.2 eV])}$$
$$(10) \quad e + O_2 \longrightarrow e + O_2(c^1\Sigma_u^-, A^3\Sigma_u^+) \quad \text{(Meta-stable Excitation [4.5 eV])}$$
$$(11) \quad e + O_2 \longrightarrow e + O(3P) + O(3P) \quad \text{(Dissociation [6.0 eV])}$$
$$(12) \quad e + O_2 \xrightarrow{B^3\Sigma_u^-} e + O(3P) + O(1D) \quad \text{(Dissociation [8.4 eV])}$$
$$(13) \quad e + O_2 \longrightarrow e + O(1D) + O(1D) \quad \text{(Dissociation [10.0 eV])}$$
$$(14) \quad e + O_2 \longrightarrow e + O_2^+ + e \qquad \text{(Ionization [12.06 eV])}$$
$$(15) \quad e + O_2 \longrightarrow e + O + O^*(3p^3P) \quad \text{(Dissociative Excitation [14.7 eV])}$$
$$(16) \quad e + O_2^+ \longrightarrow O + O \qquad \text{(Dissociative Recombination)}$$
$$(17) \quad e + O^- \longrightarrow e + O + e \qquad \text{(Electron Impact Detachment)}$$
$$(18) \quad O^- + O_2^+ \longrightarrow O + O_2 \qquad \text{(Mutual Neutralization)}$$
$$(19) \quad O^- + O_2 \longrightarrow O + O_2 + e \qquad \text{(Detachment)}$$
$$(20) \quad O^- + O_2 \longrightarrow O^- + O_2 \qquad \text{(Scattering)}$$
$$(21) \quad O_2^+ + O_2 \longrightarrow O_2 + O_2^+ \qquad \text{(Charge Exchange)}$$
$$(22) \quad O + O_2 \longrightarrow O + O_2 \qquad \text{(Scattering)}$$

The O_2 particles are assumed to be maintained uniformly in space with a 3V Maxwellian velocity distribution at room temperature ($T_N = 0.026$ eV) as a background species. All the other species are followed as particle species. Note that the electrons in this model collide with three species, two of which are particle species, i.e., the target species are not the same in all electron collisions. For purposes of the null collision method, it is easier to divide the electron collisions into three groups. Currently, we do not consider Coulomb collisions between charged particles since for low density weakly-ionized discharges, interactions between charged-neutral species are the dominant collision mechanisms.

3.2.1. Electron–O_2 collisions

The first fifteen reactions in the list are electron–O_2 collisions. The null collision method for these reactions is the same as what we had for electron–neutral reactions in argon, since the incident electrons collide off a spatially uniform background species. The cross section used for the dissociative attachment reaction is obtained
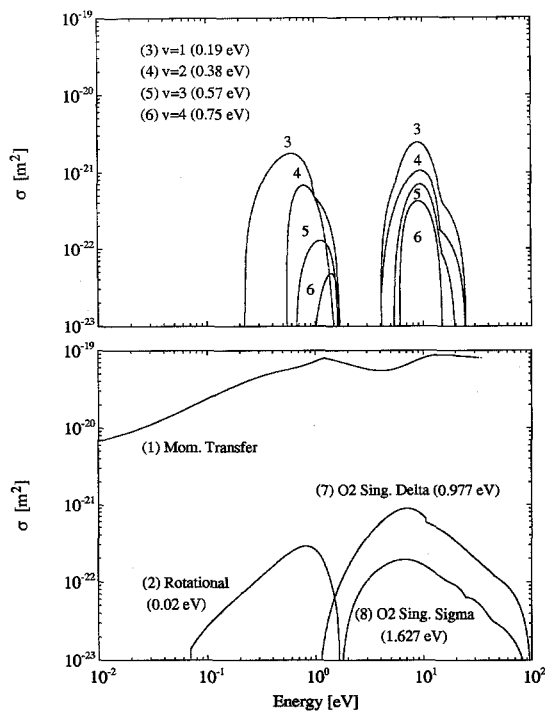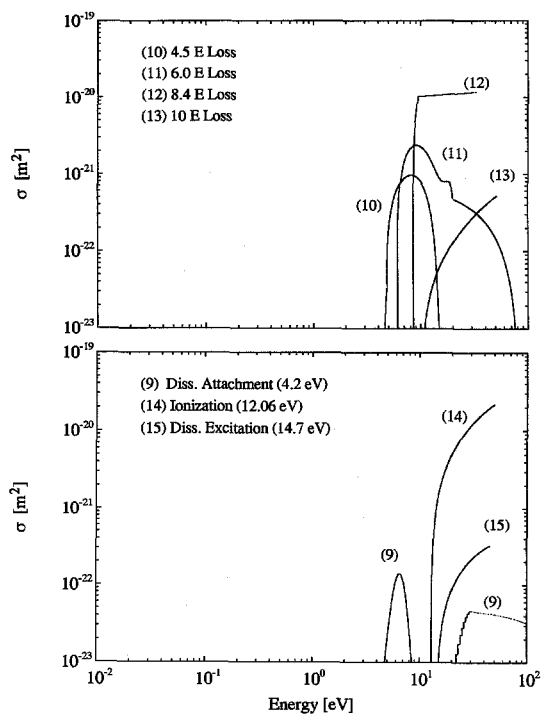
Fig. 8.

Fig. 9.

Fig. 8. The cross sections for vibrational and rotational excitations, momentum transfer, and meta-stable generation used in the model.

Fig. 9. The cross sections for electronic excitation, dissociative attachment, ionization, and dissociative excitation used in the model.

from Rapp et al. (1965) [26] and is shown in Fig. 9. The rest of cross sections are from Phelps [36,37] and are shown in Figs. 8 and 9.

The momentum transfer, along with rotational, vibrational, and electronic excitations are included in this model to serve as energy loss mechanisms for the electrons. The cross section for rotational excitation is a few orders of magnitude smaller than the other processes and is found to be a relatively unimportant reaction compared with the other electron–neutral reactions. On the other hand, the vibrational excitations are found to be very important processes and can greatly influence the shape of the electron energy distribution function (EEDF) in the system since the cross section for these processes are non-zero only over a small range of energies. Simulations have shown that the addition of vibrational excitations can lead to strongly non-Maxwellian EEDF's [38,39].

Reactions (7), (8), (10), and (11) in the list above are generation mechanisms for several types of meta-stable oxygen molecule ($a^1\Delta_g$, $b^1\Sigma_g$, $c^1\Sigma_u^-$, and $A^3\Sigma_u^+$) [37]. These reactions are important energy loss mechanisms for the electrons. Currently, we do not include two-step ionization processes (via meta-stables states). These can be included by adding the appropriate meta-stable species.

The dissociative attachment reaction is the main bulk negative-ion creation and bulk electron loss mechanisms. The incident electron loses the threshold energy of 4.2 eV and is absorbed by the oxygen molecule to form a O_2^- which then dissociates to form the fragments O and O^- [26]. The electron transition is assumed to be rapid on a nuclear time scale [28], so that one can use the Franck-Condon principle to calculate the energy of the ejected fragments. The remaining incident electron energy ($\mathcal{E}_{inc} - \mathcal{E}_{th}$) is divided between the fragments. Since the cross section has a threshold of 4.2 eV and peaks at about 6.5 eV, the created O and O^- typically

have energies of 1–2 eV. The fragments are assumed to scatter isotropically.

Reactions (12) and (13) lead to dissociation of the oxygen molecule; the incident electron loses the threshold energies of 8.4 or 10 eV to electronically excite the O_2 molecule into a higher state which will then dissociate into two O's; the created fragments are assumed to scatter isotropically. The created atoms are each born with the most probable energy of about 1–2 eV [18,37]. These reaction are the main mechanisms responsible for bulk O production.

Ionization is the sole reaction to produce the positive ions (O_2^+) in the system. The model used for ionization here is identical to that described for argon. The incident electron loses the 12 eV of threshold energy, and shares the rest of its energy with the ejected electron according to Eq. (20). We assume the function $B(\mathcal{E}_{inc})$ in Eq. (20) to have the same value as in the case of argon.

The dissociative excitation (130 nm line excitation) reaction, with a threshold of 14.7 eV, is just added as an energy sink for the high energy electrons. However, simulation has shown that this reaction is an unimportant one since its cross section is two orders of magnitude smaller than the cross section for ionization.

In all the electron–O_2 reactions (1)-(15) listed above, the incident electrons lose at least the threshold energy, and (except for the dissociative attachment reaction) scatter through angles χ and ϕ determined by Eqs. (9) and (10). We use the same electron scattering model here as for argon. As discussed previously, in an elastic collision, the incident electron loses a small amount of energy calculated from Eq. (12). Note that there are important differences between momentum transfer cross section and elastic scattering cross section for e-n collisions when using anisotropic differential scattering. If the momentum transfer collision is the elastic momentum transfer cross section then we should use isotropic scattering for χ, i.e., Eq. (26) (with Θ replaced with χ) and not Eq. (9). Alternatively, we can multiply the elastic momentum transfer cross section by [12]

$$\beta(\mathcal{E}) = \frac{\mathcal{E}\ln(1 + \mathcal{E})}{2[\mathcal{E} - \ln(1 + \mathcal{E})]} \tag{31}$$

where $\mathcal{E}$ is the energy in electronvolts, to get the elastic cross section and then use Eq. (9) to determine the scattering angle χ [12]. If the momentum transfer collision cross section is the effective momentum transfer collision cross section (as defined by Phelps [36,37]), then we need to multiply it by $\beta(\mathcal{E})$, to get the sum of all cross sections included. We must then subtract all the inelastic cross sections that have been included in the effective cross section, (e.g., vibration cross sections) to get the elastic cross section.

3.2.2. Electron–O_2^+ collisions

Since the ion temperature in the bulk plasma is typically much lower than the electron temperature, we take the ions as the target particles in this reaction. Note that the ions in this model are followed as particles, and the ion density, $n_i(\mathbf{x}, t)$ is not necessarily uniform in space or constant in time; the collision frequency is a function of space and time. Hence, in calculating the null collision cross section from Eq. (5) for this reaction, we must also take the maximum ν over all $\mathbf{x}$ each time step to obtain the instantaneous maximum collision frequency. Once the null collision frequency is calculated, we sample the electrons to determine which ones are to be recombined. If an electron is to be annihilated, we find an ion partner for the reaction by picking an ion in the same cell as the electron.

The cross section used for the dissociative recombination reaction is obtained from Akhmanov et al. (1982) [30] and is shown in Fig. 10. Although the reaction rate for this process is lower than the others, it is important to include this process in our model because the fragments in this reaction are typically created with 5–6 eV energy. The fragments are assumed to scatter isotropically. This reaction is also responsible for bulk electron–ion annihilation.

3.2.3. Electron–O^- collisions

The negative ions are mainly created in the bulk plasma through the dissociative attachment process which gives them 1–2 eV energy. In a typical plasma with a electron temperature of a few electronvolts, the negative
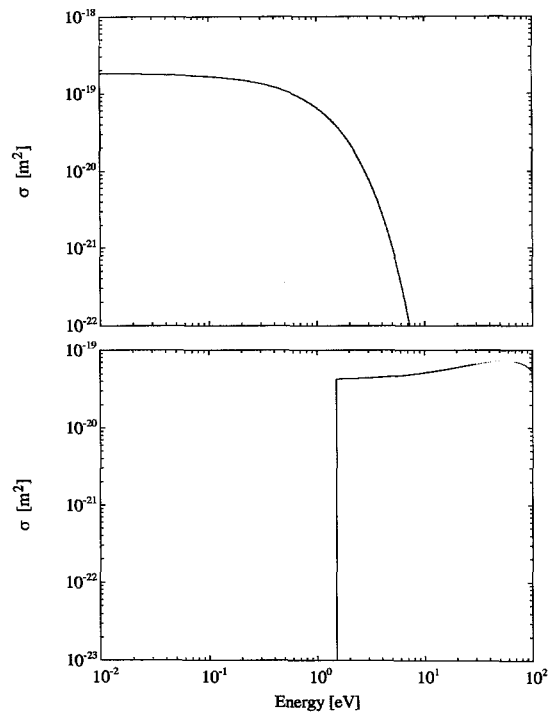
Fig. 10. The simplified average total dissociative recombination cross section (top) and electron impact detachment for O^- negative ions (bottom).

ions are clearly trapped in the bulk plasma by the ambipolar potential. Hence the negative ion loss to the walls becomes nearly zero, and the density of the O^- particles builds up in the bulk. To bring the system to equilibrium, we must introduce some other loss mechanisms for the negative ions.

Electron impact detachment is one of the reactions considered in this model to destroy the negative ions in the bulk. As in the dissociative recombination case, we take O^- which has a lower temperature in the bulk plasma than the electrons, as the target particles in this reaction. The null collision cross section must also be recalculated each time step to obtain the instantaneous maximum collision frequency, and we pick negative ion partners for the electrons in the same manner as in dissociative recombination.

The cross section used for this reaction has a threshold of 1.46 eV and peaks at about 30 eV as shown in Fig. 10 [31]. Our model for electron impact detachment is the same as for ionization. The created oxygen atom takes the identity of the negative ion and the remaining energy of the incident electron is partitioned between the scattered and ejected electrons according to Eq. (20). The function $B(\mathcal{E}_{inc})$ in Eq. (20) is assumed to be roughly 10 eV for this process.

3.2.4. $O^- - O_2^+$ collisions

Among all the negative ion loss mechanisms, mutual neutralization has the highest reaction rate and must be included. The average cross section for this process, shown in Fig. 11 peaks as the relative energy of the colliding particles approaches zero [32–35]. Although both species have roughly the same temperature as the neutrals, we chose the positive ions (O_2^+) to be the target particles and O^- as the incident projectiles. As in the dissociative recombination case, the null collision cross section is recalculated every time step to obtain the instantaneous maximum collision frequency, as the density of the target particles is a function and position and time.
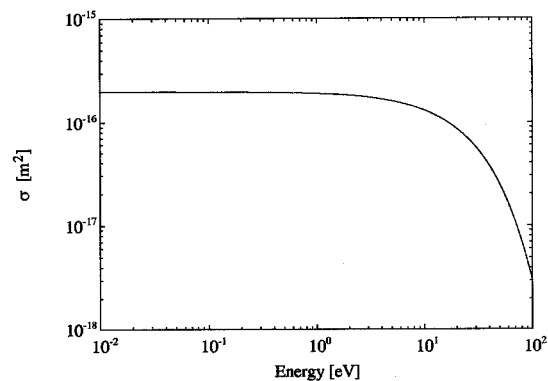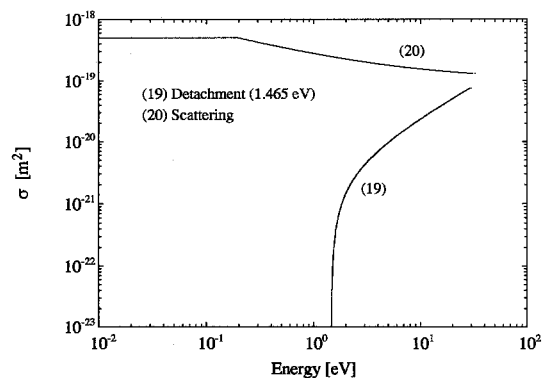
Fig. 11.

Fig. 12.

Fig. 11. The simplified average cross section for the mutual neutralization of O_2^+ and O^-.

Fig. 12. The cross sections for detachment and negative ion scattering off O_2.

This process is very similar to the ion–neutral collision reactions discussed in Section 3.1.2, because the projectiles and target particles in the collision typically have the same velocities. Thus, we find a positive ion partner in the same cell for each negative ion selected to undergo a collision, transfer the negative ion into a frame in which the positive ion is stationary, and calculate the reaction rate. The negative ion is transferred back into the normal laboratory frame if the collision is null, and recombine to create a O and a O_2, if the collision is real. In this process, the incident particles create an O_3^* which then relaxes to O and O_2. The created species have typical energies of 3-6 eV and are assumed to scatter isotropically.

3.2.5. $O^- - O_2$ collisions

Detachment and scattering of the O^- are the reactions considered in this section. The cross sections used for the scattering [41] and detachment [40] reactions are shown in Fig. 12. The target particles are the neutrals, which we have assumed to be uniformly distributed in the system. As in the previous section, these processes are also very similar to the ion–neutral collision reactions discussed in Section 3.1.2, because the velocities of both projectiles and target particles are roughly the same. Thus, each negative ion selected to undergo a collision, in the null collision scheme, is transferred into a frame in which the neutral is stationary, goes through a collision, and is transferred back into the normal laboratory frame.

The scattering process is assumed to be a hard sphere collision. The incident O^- scatters through an angle χ in the laboratory frame, and transfers some momentum to the neutral particle. The energy of the scattered O^- can be found through the energy and momentum conservation equations to be

$$\mathcal{E}_{scat} = \mathcal{E}_{inc} \left(\frac{\cos \chi + \sqrt{\cos^2 \chi + 3}}{3} \right)^2 \tag{32}$$

where $\mathcal{E}_{scat}$ and $\mathcal{E}_{inc}$ are the scattered and incident energies. Note that since the negative ions and the neutrals do not have the same mass ($M_{O_2}/M_{O^-} = 2$), this expression differs from what we obtained for argon ion scattering in Eq. (25).

The angle χ can be determined by assuming the scatterings to be uniform and isotropic in the center-of-mass frame, which gives

$$\cos \Theta = 1 - 2R \tag{33}$$

where Θ is the scattering angle in the center-of-mass frame and R is a random number ($R \in [0,1]$). The relationship between the scattering angles χ and Θ is [22]

$$\tan \chi = \frac{\sin \Theta}{\gamma + \cos \Theta} \tag{34}$$

where γ is the mass ratio; in this case $\gamma = M_{O^-}/M_{O_2} = 1/2$. Solving this for χ gives

$$\tan \chi = \frac{\sqrt{R(1-R)}}{0.75 - R} \tag{35}$$

where R is yet another random number ($R \in [0,1]$).

As we discussed before, the negative ions are typically trapped in the bulk plasma by the time-average potential. This scattering process is then the main mechanism for the negative ions to lose energy and thermalize with the neutrals.

The cross section for the detachment process has a threshold at 1.46 eV. This process can serve as a bulk negative ion loss mechanism in the system. However, as a result of scattering collisions, the negative ion temperature in the bulk, T_-, is on the order of T_N, the O_2 temperature, which makes it very hard for the negative ions to get over the threshold energy for detachment. If a detachment collision does occur, an electron will be created with a very low energy and is assumed to scatter isotropically. The more massive particles in this process, the created O and the scattered O_2, leave with most of the incident energy. Since the remaining energy is typically small, it is not crucial to derive an accurate model for the energy partition. A simple energy partitioning scheme would be to divide up the energy based on the mass ratio of the O and O_2.

3.2.6. $O_2^+ - O_2$ collisions

Our model for positive ion–neutral collision is identical to the charge exchange model derived for argon ions in Section 3.1.2. The cross section is shown in Fig. 13 and has no threshold [42]. The positive ion is transferred into a frame in which the neutral is at rest. The ion then goes through a collision and finally is transferred back into the laboratory frame. This process is responsible for thermalization of positive ions with O_2. As in $Ar^+ - Ar$ collisions, the separation between charge exchange and elastic scattering (not included here for $O_2^+ - O_2$) is an artificial construct. These collisions can be modeled more accurately if a fit to the differential cross section for $O_2^+ - O_2$ collisions is known.

3.2.7. $O - O_2$ collisions

The O atoms are created primarily through dissociation, with typical energies of 1-3 eV. They are also created through dissociative attachment, dissociative recombination, electron impact detachment, and mutual neutralization with energies of 1-5 eV. In the absence of any other collisions, the O atoms are unaffected by the local electric field would simply drift to the walls.

Currently, scattering is the only collision which the O atoms are allowed to have in the model. The scattering event is assumed to be a hard sphere collision which makes our model for this process identical to the scattering collision for the negative ions discussed in Section 3.2.5. The cross section is shown in Fig. 14 [42]. The O is scattered through an angles χ and ϕ determined by Eqs. (35) and (10), and loses energy to the neutrals, O_2, according to Eq. (32).

4. Comparisons between PIC-MCC simulations and laboratory measurements in an argon RF discharge

The Monte Carlo procedure described above is implemented in a one-dimensional electrostatic code called PDP1 [15]. PDP1 was used to simulate a one-dimensional capacitively-coupled argon RF discharge symmetrically driven at 13.56 MHz, and the simulation results were compared with the laboratory measurements of
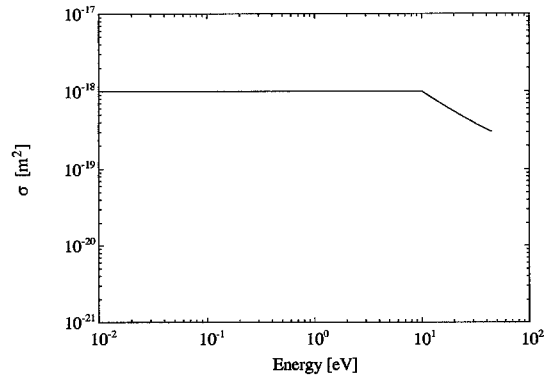
Fig. 13.   Fig. 14.

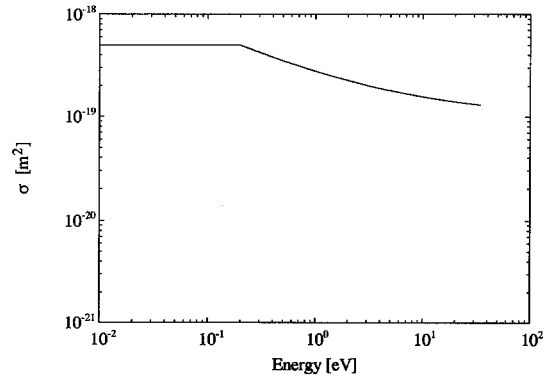Fig. 13. The total charge exchange cross section between O_2^+ and O_2.

Fig. 14. The total cross section for scattering of O off of O_2 in an oxygen plasma.

Godyak et al. [17]. This comparison has been reported previously [15]. The experimental system was very carefully designed to drive the discharge symmetrically. The discharge, confined radially by a Pyrex glass cylinder with a diameter of 14.3 cm, had a cross sectional area of 160 cm^2. All probe measurements were made in the mid-plane on the axis of the discharge which occurred between two parallel aluminum electrodes. We compare results from PDP1 with those measured by Godyak et al. in an argon RF discharge with a gap separation of 2 cm, and discharge current of 2.56 mA/cm^2. Fig. 15 shows the electron energy probability function (EEPF) obtained from PDP1 at the gas pressure of 100 mTorr. We refer to the effective temperature and density associated with the low-energy electrons as T_l and n_l (labeled T_1 and n_1 in Fig. 10 of Godyak et al. [17]). We also use T_h and n_h for the same quantities associated with the high energy group (labeled T_2 and n_2 in Fig. 10 of Godyak et al. [17]). The effective temperature of the high energy electrons obtained from PDP1 is in excellent agreement with Godyak's measurement, while the temperature of the low energy electrons from PDP1 is slightly higher. This higher temperature may be due to numerical heating (so-called self-heating) [16,43,15] of the electrons in PDP1.

The EEPFs measured by Godyak et al. [17] (in Fig. 16 of [17]) also vary considerably in detail, being convex at high pressures and concave at low pressures. For the 2 cm gap discharge, the transition occurred at a neutral gas pressure of roughly 350 mTorr. Simulation results from PDP1, shown in Fig. 16, display the same convex-concave transition from low gas pressures to high pressures. The change in the shape of the EEPFs is proposed by Godyak et al. [17] to be a transition in the electron heating-mode from predominantly collisionless heating at low-pressures to collisional heating at high pressures. This point was confirmed by Vahedi et al. [15].

The effective temperatures for the low and high energy electron groups obtained from simulation with and without secondaries, shown in Fig. 17, are in very good agreement with those measured by Godyak et al. [17]. The effective bulk temperatures obtained from simulation with secondary electron emission are slightly, but not significantly, higher than in cases with no secondaries. At higher pressures, where the EEPFs lose their bi-Maxwellian profiles, the effective temperature of both groups of electrons tends to be the same.

5. PIC-MCC simulations of capacitively-coupled oxygen RF discharges

Note that the reactions included for oxygen in Sec. 3.2 does not include ionization of atomic oxygen. Hence, this model is adequate only for modeling weakly dissociated oxygen discharges in which one would expect
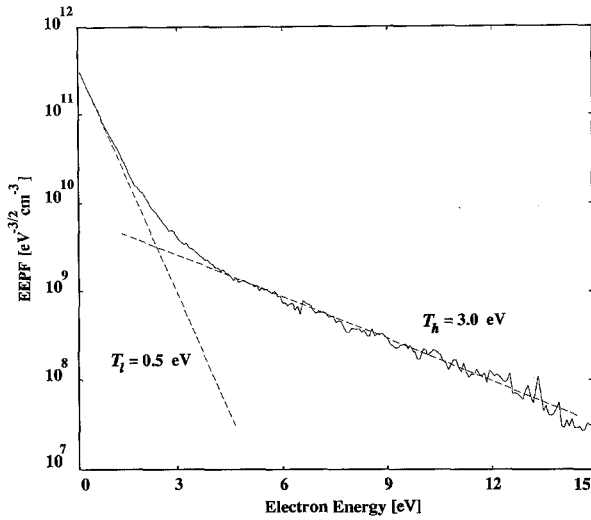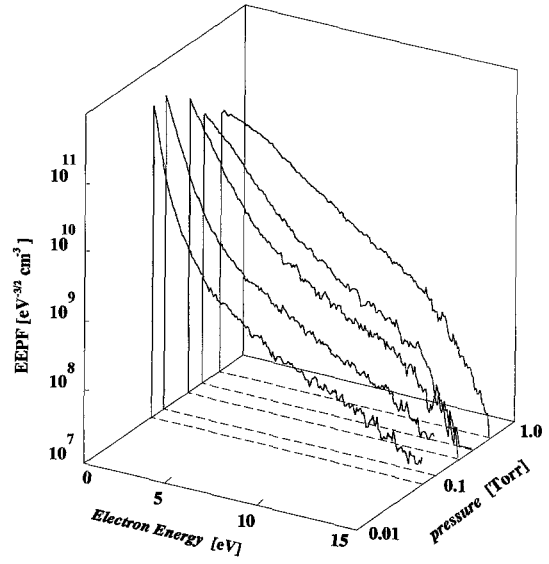
Fig. 15.   Fig. 16.

Fig. 15. The EEPF obtained from a current driven argon RF discharge simulation driven at 13.56 MHz with a discharge current of 2.56 mA/cm² in a 2 cm gap and a neutral pressure of 100 mTorr. The dashed lines represent the two temperature Maxwellian distribution of the discharge.

Fig. 16. The EEPFs from a current-driven argon RF discharge simulations running at 13.56 MHz with a 2 cm gap over a range of pressures.

O_2^+ to be the dominant positive ion species, and O_2 as the dominant neutral species in the discharge. However, as the fractional dissociation (n_O/n_{O_2}) scales directly with the electron density, the low fractional dissociation assumption is typically justified in conventional capacitive RF discharges where the electron density is relatively low $(n_e \sim 10^9 \text{ cm}^{-3})$. For modeling high density sources where the electron density is two to three orders of magnitude higher $(n_e \sim 10^{12} \text{ cm}^{-3})$, one needs to also include reactions involving O^+.

We incorporated the Monte Carlo scheme described in Section 3.2 in PDP1 to model a capacitively coupled oxygen discharge at relatively low input powers. The simple scaling law developed by Lichtenberg et al. [38] for electronegative discharges predicts that, at low input powers and relatively high pressures, the ratio of the negative ion density to the electron density at the center of the discharge is greater than one, i.e., $\alpha_0 = n_-(0)/n_e(0) > 1$, where $n_- = n_{O^-}$. Simulation results for α_0 and n_+, positive ion density, are plotted in Fig. 18 versus the input power for two neutral pressures of 10 and 50 mTorr. Note that as the input power increases, ion and electron densities increase, while α_0 decreases, which verifies the scaling of Lichtenberg et al. [38].

The simple model of Lichtenberg et al. also predicts the spatial density profiles of the electrons, positive ions and negative ions in the system. A comparison of time-averaged density profiles obtained from PDP1 simulation and the analytic profiles of Lichtenberg et al. is shown in Fig. 19 at 50 mTorr, 0.02 W/cm², and a gap size of 4.5 cm. Because the system is symmetric, Fig. 19 shows the density profiles for only half of the system.

We can divide the system into three regions, from the center of the symmetric discharge to the driven electrode. First is a central electronegative region where $n_-(x)/n_e(x) > 1$, and potential variations are on the order of the negative ion temperature $(T_- \sim T_+ \ll T_e)$. In this region, due to small potential variations, the electron density is essentially constant. Once the potential variations become larger than the negative ion temperature the density of negative ions becomes negligible and we enter an intermediate electropositive region.

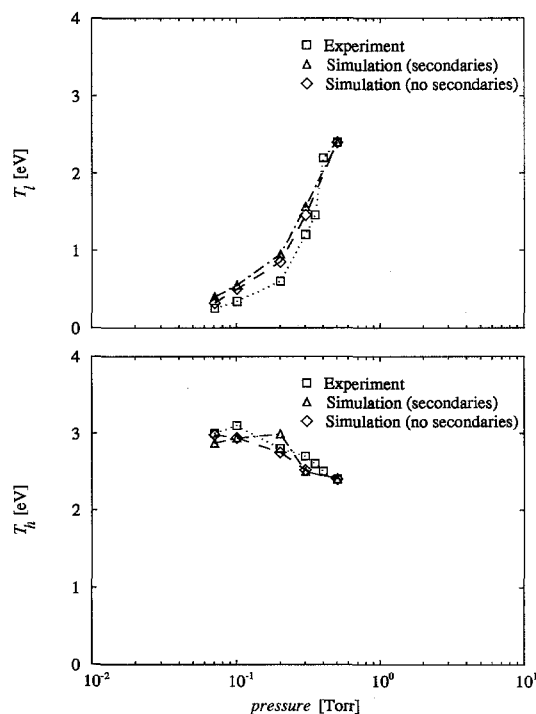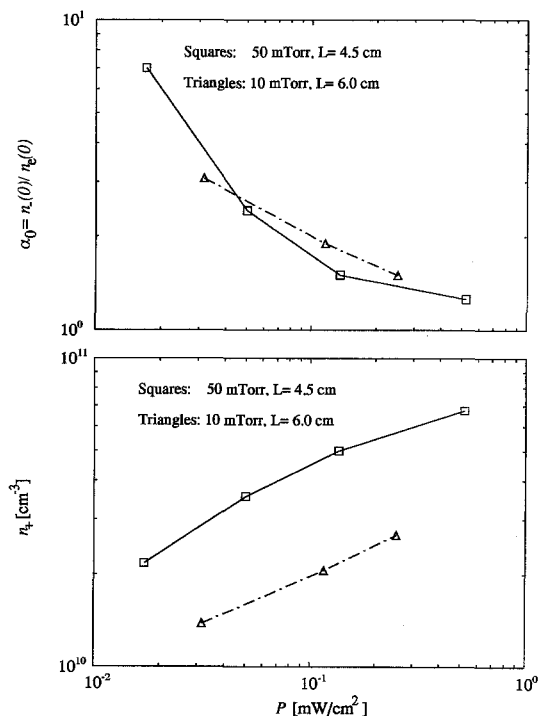Fig. 17.   Fig. 18.

Fig. 17. Comparison of the effective temperatures of the low and high energy electron groups in the system in a 2 cm gap current-driven argon RF discharge. The squares are measurements by Godyak et al. [17]; the diamonds are simulation results without secondary electron emission; the triangles are simulation results with secondary electron emission.

Fig. 18. The ratio of negative ion to electron density (top) and positive ion density (bottom) as a function of input power for two neutral pressures of 10 and 50 mTorr. The length of the system was chosen to be 4.5 cm for the 50 mmTorr case and 6.0 cm for the 10 mTorr case.

In this region, the usual ambipolar fields retard the electrons and accelerate the ions to arrive into the sheath with energies on the order of the electron temperature. The last region is a large capacitive sheath which further accelerate the ions toward the electrode. Note that the simple profiles of Lichtenberg et al. compare favorably with the time-averaged density profiles from PDP1 simulation.

As the plasma becomes more electronegative, the central region expands at the expense of the electropositive region to the limit where the Bohm criterion is modified to account for the presence of negative ions near the plasma sheath boundary. On the other hand as the negative ion density decreases, the central region shrinks and the negative ions become confined to the very center of the discharge. Our reasoning here assumes that the negative ions are in a Boltzmann equilibrium with the potential and that the negative ion temperature is much smaller than the electron temperature, which has been verified by PDP1 simulations.

Fig. 20 show two typical electron energy distribution functions in an oxygen capacitively coupled discharge. Both EEDFs at 10 and 50 mTorr are non-Maxwellian. The non-Maxwellian feature of EEDFs has also been seen in Boltzmann simulations of molecular gases and is largely due to relatively large cross sections of low energy inelastic collisions, such as vibrational excitations. Electron sheath heating at low pressures [17] can also distort the EEDFs.
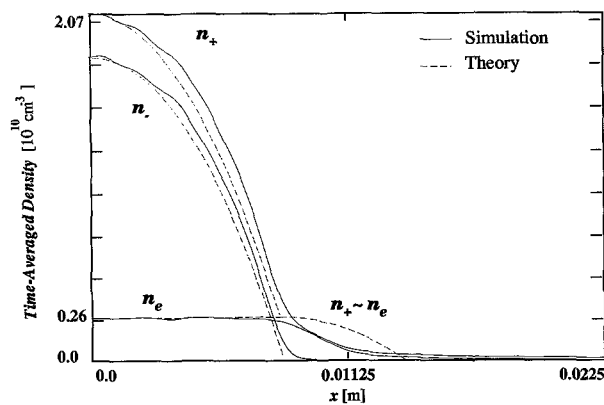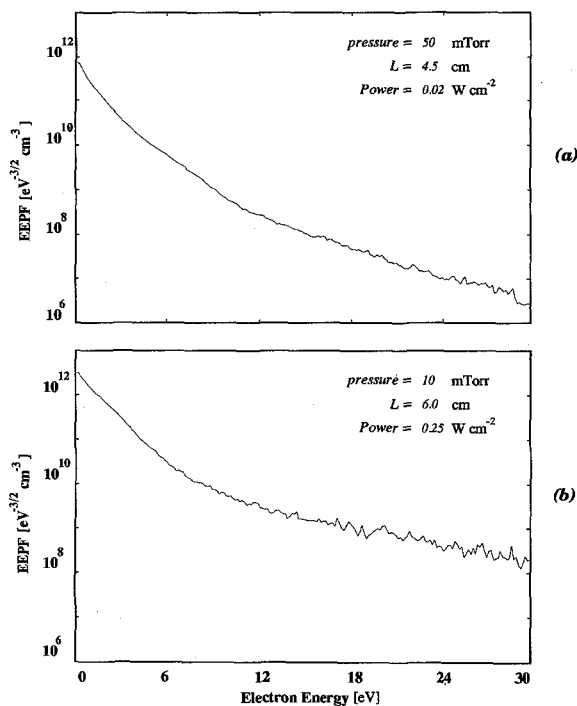
Fig. 19.

Fig. 20.

Fig. 19. Density profiles of electrons, positive and negative ions in a capacitively coupled oxygen RF discharge at 50 mTorr, 0.02 W/cm^2, and a gap size of 4.5 cm. Because the system is symmetric, the density profile is plotted for only half of the system.

Fig. 20. Electron energy distribution functions obtained from simulations of capacitively coupled oxygen RF discharges at 10 and 50 mTorr.

6. Conclusions

A Monte Carlo collision (MCC) handler, including the null collision method, has been developed as an addition to the PIC scheme for modeling self-sustained discharges. The full three-dimensional character of a collision is modeled with three velocity components. A subset of typical reactions present in laboratory gas discharges is modeled for argon, an electropositive gas, and oxygen, an electronegative gas. The addition of the null collision method makes the scheme computationally more efficient. as the collision frequency increases, so does the fraction of particles undergoing collisions, and more time is spent in the MCC handler (see Fig. 1). Typically, the fraction of time taken up by the MCC handler per time step is about 10–20%. This Monte Carlo scheme is implemented in PDP1 [15], a one-dimensional code electrostatic code, and PDP2 [44] a two-dimensional electrostatic code for simulating processing plasmas. Comparisons of argon simulation results with laboratory measurements of Godyak et al. are very favorable.

7. Acknowledgements

discussions with I.J. Morey, J.P. Verboncoeur, C.K. Birdsall, D.B. Graves, J.R. Hiskes, R. Procassini, and T.D. Rognlien.

References

[1] D.B. Graves and K.F. Jensen, IEEE Trans. Plasma Sci. PS-14 (1986) 78.
[2] J.P. Boeuf, Phys. Rev. A 36 (1987) 2782.
[3] E. Gogolides, J.P. Nicolai and H.H. Sawin, J. Vac. Sci. Technol. A 7 (1989) 1001.
[4] S.R. Hunter, Aust. J. Phys. 30 (1977) 83.
[5] J.P. Boeuf and E. Marode, J. Phys. D 15 (1982) 2169.
[6] Y. Kaufman, J. Phys. D 21 (1988) 442.
[7] M.J. Kushner, J. Appl. Phys. 58 (1985) 4024.
[8] M.J. Kushner, J. Appl. Phys. 54 (1983) 4958.
[9] B.E. Thompson, H.H. Sawin and D.A. Fisher, J. Appl. Phys. 63 (1988) 2241.
[10] S.L. Lin and J.N. Bardsley, J. Chem. Phys. 66 (1977) 435.
[11] M. Surendra, D.B. Graves and I.J. Morey, Appl. Phys. Lett. 56 (1990) 1022.
[12] M. Surendra, D.B. Graves and G.M. Jellum, Phys. Rev. A 41 (1990) 1112.
[13] T. Holstein, Phys. Rev. 70 (1946) 367.
[14] C.K. Birdsall, IEEE Trans. Plasma Sci. 19 (1991) 65.
[15] V. Vahedi, C.K. Birdsall, M.A. Lieberman, G. DiPeso and T. D. Rognlien, Plasma Source Sci. Technol. 2 (1993) 261, 273.
[16] C.K. Birdsall and A.B. Langdon, Plasma Physics Via Computer Simulation (Adam Hilger, Bristol, 1991).
[17] V.A. Godyak, R.B. Piejak and B.M. Alexandrovich, Plasma Sources Sci. Technol. 1 (1992) 36.
[18] A.E. Bell and H. V. Boeing, Fundamentals of plasma chemistry and technology (Technomic Pub. Co., 1988).
[19] M. Surendra and D.B. Graves, IEEE Trans. Plasma Sci. 19 (1991) 144.
[20] D. Vender and R.W. Boswell, IEEE Trans. Plasma Sci. 18 (1990) 725.
[21] T.J. Sommerer, W.N.G. Hitchen, R.E.P. Harvey and J. E. Lawler, Phys. Rev. A 43 (1991) 4452.
[22] E.W. McDaniel, Atomic Collisions (Wiley, New York, 1989).
[23] C.B. Opal, W.K. Peterson and E.C. Beaty, J. Chem. Phys. 55 (1971) 4100.
[24] W.H. Cramer, J. Chem. Phys. 30 (1959) 641.
[25] M.L. Vestal, C.R. Blakley and J.H. Futrell, Phys. Rev. A 17 (1978) 1337.
[26] D. Rapp and D.D. Briglia, J. Chem. Phys. 43 (1965) 1480.
[27] D. Rapp and D.D. Briglia, J. Chem. Phys. 43 (1965) 1464.
[28] B.M. Smirnov, Negative Ions (McGraw-Hill, New York, 1982).
[29] H. Myers, J. Phys. B 393 (1969).
[30] S.A. Akhmanov Jr., K.S. Kloponskii and A.P. Osipov, Sov. Phy. JETP 56 (1982) 936.
[31] G.C. Tisone and L.M. Branscomb, Phys. Rev. 170 (1966) 15.
[32] B. Peart and S.J. Foster, J. Phys. B 20 (1987) 691.
[33] W.H. Aberth and J.R. Peterson, Phys. Rew. 1 (1970) 158.
[34] H.S.W. Massey, Negative Ions (Cambridge University Press, Cambridge, 1976).
[35] S. Szucs, M. Karemera, M. Terao and F. Brouillard, J. Phys. B 17 (1984) 1613.
[36] A.V. Phelps, JILA Information Center Report No. 28, University of Colorado, Boulder, CO (1985).
[37] S.A. Lawton and A.V. Phelps, J. Chem. Phys. 69 (1978) 1055.
[38] A.J. Lichtenberg, V. Vahedi, M.A. Lieberman and T.D. Rognlien, J. Appl. Phys. 75 (1994) 2339.
[39] M.M. Turner and M.B. Hopkins, Phys. Rev. Lett. 69 (1992) 3511.
[40] A.E. Roche and C.C. Goodyear, J. Phys. B 2 (1969) 191.
[41] E.E. Muschlitz Jr., Proc. of the Fourth Inter. Conf. on Ion. Phenom. in Gases, Upssala (1959).
[42] E.A. Mason and E.W. McDaniel, Transport Properties of Ions in Gases (Wiley, New York, 1988).
[43] R.W. Hockney, J. Comput. Phys. 8 (1971) 19.
[44] V. Vahedi, G. DiPeso, T.D. Rognlien and C.K. Birdsall, Phys. Fluids B 5 (1993) 2719.